

# A weak lensing analysis of the Abell 2163 cluster. ★

M. Radovich<sup>1</sup>, E. Puddu<sup>1</sup>, A. Romano<sup>1</sup>, A. Grado<sup>1</sup>, and F. Getman<sup>2</sup>

<sup>1</sup> INAF - Osservatorio Astronomico di Capodimonte, via Moiariello 16, I-80131, Napoli

<sup>2</sup> INAF - VSTceN, via Moiariello 16, I-80131, Napoli

received; accepted

## ABSTRACT

**Aims.** This paper is aimed at measuring the main physical properties (mass, velocity dispersion, and total luminosity) of the cluster Abell 2163.

**Methods.** Weak lensing analysis is applied to a deep, one square degree *r*-band CFHT-Megacam image of the Abell 2163 field. The observed shear is fitted with Single Isothermal Sphere and Navarro-Frenk-White models to obtain the velocity dispersion and the mass, respectively; in addition, aperture densitometry is also used to provide a mass estimate at different distances from the cluster centre. The luminosity function is finally derived, allowing to estimate the mass/luminosity ratio.

**Results.** Previous weak lensing analyses performed at smaller scales produced somewhat contradictory results. The mass and velocity dispersion obtained in the present paper are compared and found to be in good agreement with the values computed by other authors from X-ray and spectroscopic data.

**Key words.** Galaxies: clusters: individual Abell 2163 – Galaxies: fundamental parameters – Cosmology: dark matter

## 1. Introduction

Abell 2163 is a cluster of galaxies at  $z=0.203$  with richness class 2 (Abell et al. 1989) and without any central cD galaxy (Fig. 1). It is one of the hottest clusters known so far with an X-ray temperature of 14 keV and an X-ray luminosity of  $6 \times 10^{45}$  erg  $s^{-1}$  based on Ginga satellite measurements (Arnaud et al. 1992). Elbaz et al. (1995) used ROSAT/PSPC and GINGA data to map the gas distribution and showed that the gas extends to at least 4.6 Mpc or 15 core radii, with an elongation in the east-west direction; they estimated a total mass  $(1.43 \pm 0.05) \times 10^{15} M_{\odot}$  ( $h = 0.5$ ) within that radius, that is 2.6 times greater than the total mass of Coma. The corresponding gas mass fraction,  $0.1 h^{-3/2}$ , is typical of other rich clusters. The peak of the X-ray emission was found to be close to a bright elliptical galaxy ( $\alpha = 16^h 15^m 49.0^s$ ,  $\delta = -06^{\circ} 08' 41''$ ), as confirmed by later X-ray observations (Martini et al. 2007). Two faint gravitational arcs are visible close to this galaxy (Fig. 1); the redshift of the source galaxies is  $z_s \sim 0.73$  (Miralda-Escude & Babul 1995). The gas velocity dispersion is also very high,  $\sigma = 1680$  km  $s^{-1}$  (Arnaud et al. 1994); Martini et al. (2007) derived a velocity dispersion  $\sigma = 1381 \pm 324$  km/s from spectroscopic data.

ASCA observations of Abell 2163 (Markevitch et al. 1996) show a quick drop of the temperature at large radii, strongly constraining the total mass profile, assumed to follow a simple parametric law (Markevitch et al. 1996) and considerable gas temperature variations in the central 3-4 core radii region. The total mass derived inside  $0.5h^{-1}$  Mpc is  $4.3 \pm 0.5 \times 10^{14} h^{-1} M_{\odot}$ , while inside  $1.5h^{-1}$  Mpc it is  $1.07 \pm 0.13 \times 10^{15} h^{-1} M_{\odot}$ .

Send offprint requests to: M. Radovich: radovich@oacn.inaf.it

\* Based on observations obtained with MegaPrime/MegaCam, a joint project of CFHT and CEA/DAPNIA, at the Canada-France-Hawaii Telescope (CFHT) which is operated by the National Research Council (NRC) of Canada, the Institut National des Sciences de l'Univers of the Centre National de la Recherche Scientifique of France, and the University of Hawaii.

Abell 2163 is remarkable also in the radio band: as first reported by Herbig & Birkinshaw (1994), it shows a very extended and powerful radio halo. Feretti et al. (2001) further investigated the radio properties of the cluster. In addition to its size ( $\sim 2.9$  Mpc), the halo is slightly elongated in the E-W direction: the same elongation is also seen in the X-ray.

All these evidences show that this cluster is unrelaxed and have been interpreted as signatures of a recent or an ongoing merger of two large clusters (Elbaz et al. (1995), Feretti et al. (2004)). This has been confirmed by the recent analysis by Maurogordato et al. (2008), who explain the properties of Abell 2163 in terms of a recent merging, with the main component lying in the EW direction and a further northern subcluster (Abell 2163-B) belonging to the same complex. They also used optical and spectroscopic data to compute the virial mass,  $M_{\text{vir}} = (3.8 \pm 0.4) \times 10^{15} M_{\odot}$  and the gas velocity dispersion,  $\sim 1400$  km  $s^{-1}$ .

Squires et al. (1997) first performed a weak lensing analysis of Abell 2163 using a  $2048 \times 2048$  CCD at the prime focus of the Canada-France Hawaii Telescope (CFHT). They mapped the dark matter distribution up to  $7'$  ( $\sim 1h^{-1}$  Mpc); the mass map shows two peaks, one close to the elliptical galaxy, the other at  $3'$  W. The mass obtained by weak lensing alone was a  $\sim 2$  factor lower than the value derived by X-ray data: they explained the mass discrepancy by the extension of the mass distribution, larger than the size of the CCD; taking into account this effect, a reasonable agreement is achieved between the mass determined by X-ray and weak lensing. A fit of the shear profile with that expected from a singular isothermal model gave a velocity dispersion  $\sigma = 740$  km  $s^{-1}$ , lower than the expected  $> 1000$  km  $s^{-1}$  value.

A more recent weak lensing analysis of Abell 2163 was done by Cypriano et al. (2004) using FORS1 at VLT in the imaging mode. They obtained a higher velocity dispersion  $\sigma = 1021 \pm 146$  km  $s^{-1}$ . They explained the difference by the fact that

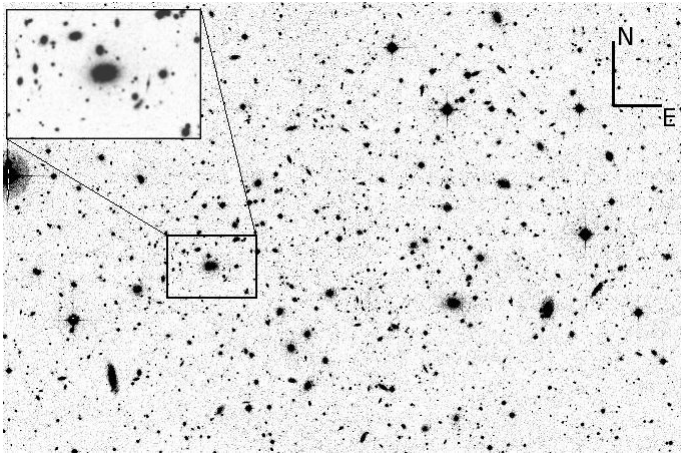


**Fig. 1.**  $r$ -band image of the Abell 2163 field. The zoomed image shows the bright elliptical galaxy identified as the centre of the cluster from the X-ray maps: also visible are the faint gravitational arcs.

Squires et al. (1997) used a bright cut ( $V > 22$  mag,  $I > 20.5$  mag) for the selection of background galaxies, whereas they chose  $R > 23.3$  mag.

Wide-field cameras, such as the ESO Wide-Field Imager (WFI) with a field of view of  $34' \times 33'$ , and more recently the Megacam camera mounted at the CFHT ( $\sim 1$  square degree), are particularly well suited for the weak lensing study of clusters as they allow to sample the signal well beyond their size. We used here public archive data available for Abell 2163 with the latter instrument for a new weak lensing analysis of this cluster; the luminosity function of the galaxies in the cluster is also derived.

This paper is organized as follows. Section 2 describes the data and the steps followed for the reduction. The weak lensing analysis and the determination of the mass is discussed in sect. 3. Finally, the cluster luminosity function is derived in Section 4, and hence the mass to luminosity ratio is computed.

We adopt  $H_0 = 70$  km s $^{-1}$ ,  $\Omega_\Lambda = 0.7$ ,  $\Omega_m = 0.3$ , giving a linear scale of 3.34 kpc'' at the redshift of Abell 2163.

## 2. Observations and data reduction

Abell 2163 was observed in 2005 with the Megacam camera at the 3.6m Canada-France Hawaii Telescope in the  $r$  band, with a total exposure time of 2.7hr. The prereduced (bias and flat-field corrected) images were retrieved from the Canadian Astronomy Data Centre archive (<http://www2.cadc-ccda.hia-ihc.nrcnrc.gc.ca/cadc/>). Before coadding the different exposures, it was necessary to remove the effect of distortions produced by the optics and by the telescope. This was done using the `ASTROMC` package, which is a porting to C++ of the `ASTROMETRIX` package described in Radovich et al. (2004): we refer to this paper for further details. Basically, for each image an astrometric solution is computed taking as reference the USNO-A2 catalog, but also taking into account the position of the same sources in other images. It follows that the absolute accuracy with respect to the USNO-A2 is  $\sim 0.3''$ , that is the nominal accuracy of the reference catalog; the internal accuracy of the same sources detected in different images is much lower ( $\sim 0.01''$ ), which is important in order to optimize the PSF in the final coadded image. At the same time, `ASTROMC` computes for each exposure an offset to the zero point to take into account changes e.g. in the transparency of the atmosphere, relative to one exposure

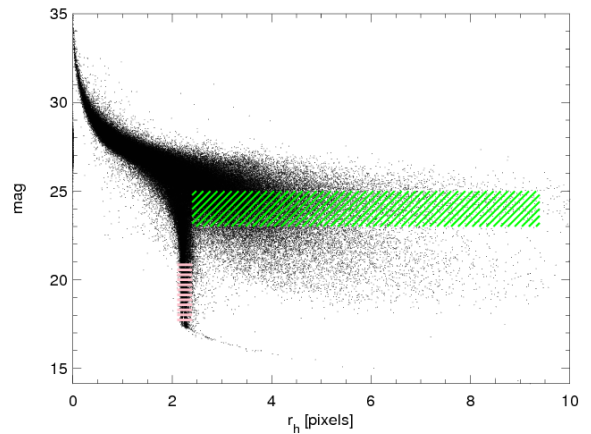


**Fig. 2.** Selection of galaxies used for the lensing analysis (area with oblique lines) and of the stars used for the PSF correction (area with horizontal lines) in the CFHT-Megacam  $r$ -band image;  $r_h$  is the half-light radius.

taken as reference. Photometric zero points are already given in the header of the images; Table 1 summarizes the photometric parameters. All the images were then resampled according to the astrometric solution and coadded together using the `SWARP` software developed by E. Bertin (<http://terapix.iap.fr/>). Finally, catalogs of sources were extracted using `SEXTRACTOR`. Galaxies and stars were selected by the analysis of the  $r_h$  vs. magnitude diagram, where  $r_h$  is the half-light radius (Fig. 2). The coadded image was inspected to look for regions with spikes and halos around bright stars. Such regions were masked on the image with `DS9` (<http://hea-www.harvard.edu/RD/ds9/>) and sources inside them were discarded from the catalog. In addition, we did not use the outer part of the image, where the PSF is rapidly degrading. The residual available area is 1775 arcmin $^2$ .

Finally, we note that Abell 2163 lies in a region with high Galactic extinction: from the maps by Schlegel et al. (1998), using the code available at <http://www.astro.princeton.edu/~schlegel/dust/> we get  $0.27 < E(B - V) < 0.43$  in the field, with an average value  $E(B - V) = 0.35$ . Such change is significantly higher than the typical uncertainty on  $E(B - V)$  ( $\sim 16\%$ , Schlegel et al. (1998)): it is therefore more appropriate to correct the magnitude of each galaxy for the extinction value at its position, rather than using the same average value.

## 3. Weak lensing analysis

Weak lensing relies on the accurate measurement of the average distortion produced by a distribution of matter on the shape of background galaxies. As the distortion is very low, the removal of systematic effects, in particular the contribute to the Point Spread Function (PSF) both from the telescope and from the atmosphere, is of crucial importance. Up to now, most of the published weak lensing results adopt the so-called KSB approach proposed by Kaiser et al. (1995) and Luppino & Kaiser (1997).

In the KSB approach, for each source the following quantities are computed from the moments of intensity distribution: the observed ellipticity  $e$ , the smear polarizability  $P^{\text{sm}}$  and the shear polarizability  $P^{\text{sh}}$ . It is assumed that the PSF can be described as the sum of an isotropic component which circularizes the images (seeing) and an anisotropic part introducing a systematic

Zero point	Color term	Extinction coeff.	$A_r$	$m_{AB}(\sigma = 3)$	$m_{AB}(\sigma = 5)$	$m_{AB}(\sigma = 10)$
26.1	$0.00 \times (g-r)$	0.10	0.92	27.0	26.4	25.5

**Table 1.** Photometric calibration terms and magnitude limits computed for point-like sources at different signal to noise ratios in the CFHT-Megacam  $r$ -band.  $A_r$  is the average Galactic extinction, for  $E(B - V) = 0.35$ . Megacam zero points are defined so that magnitudes are already in the AB system, and are here given so that the airmass is 0.

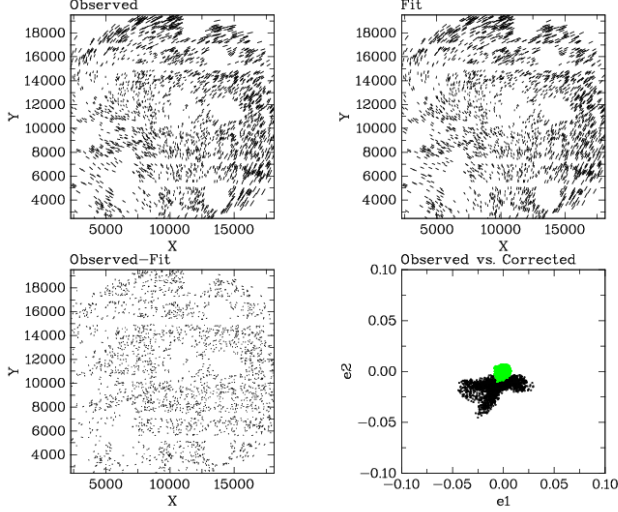


**Fig. 3.** PSF correction: the first three panels show the spatial pattern of the observed, fitted and residual ellipticities of stars: a scaling factor was applied for display purposes;  $X$  and  $Y$  are the pixel coordinates in the image. The last panel shows the observed vs. corrected ellipticities.

contribute. We summarize here the main points and refer e.g. to Kaiser et al. (1995), Luppino & Kaiser (1997) and Hoekstra et al. (1998) for a more detailed discussion. The intrinsic ellipticity  $e_s$  of a galaxy is related to the observed one,  $e_{\text{obs}}$ , and to the shear,  $\gamma$ , by:

$$e_{\text{obs}} = e_s + P^\gamma \gamma + P^{\text{sm}} p. \quad (1)$$

The term  $p$  describes the effect of the PSF anisotropy (starred terms indicate that they are derived from measurement of stars):

$$p = e_{\text{obs}}^* / P^{\text{sm}*}. \quad (2)$$

As this quantity changes with the position in the image, it is necessary to fit it using e.g. a polynomial so that it can be extrapolated to the position of the galaxy. In our case, we see that a polynomial of order 2 is sufficient.

The term  $P^\gamma$ , introduced by Luppino & Kaiser (1997) as the *pre-seeing shear polarizability*, describes the effect of the seeing and is defined as:

$$P^\gamma = P^{\text{sh}} - P^{\text{sm}} \frac{P^{\text{sh}*}}{P^{\text{sm}*}}. \quad (3)$$

As discussed by Hoekstra et al. (1998), the quantity  $\frac{P^{\text{sh}*}}{P^{\text{sm}*}}$  should be computed with the same weight function used for the galaxy to be corrected. For this reason, the first step is to compute it using weight functions of size drawn from a sequence of bins in the half-light radius  $r_h$ . In many cases,  $\frac{P^{\text{sh}*}}{P^{\text{sm}*}}$  can be assumed to be constant across the image and be computed from the average of the values derived from the stars in the field. In the case of the Megacam image, considering the size of the field we preferred

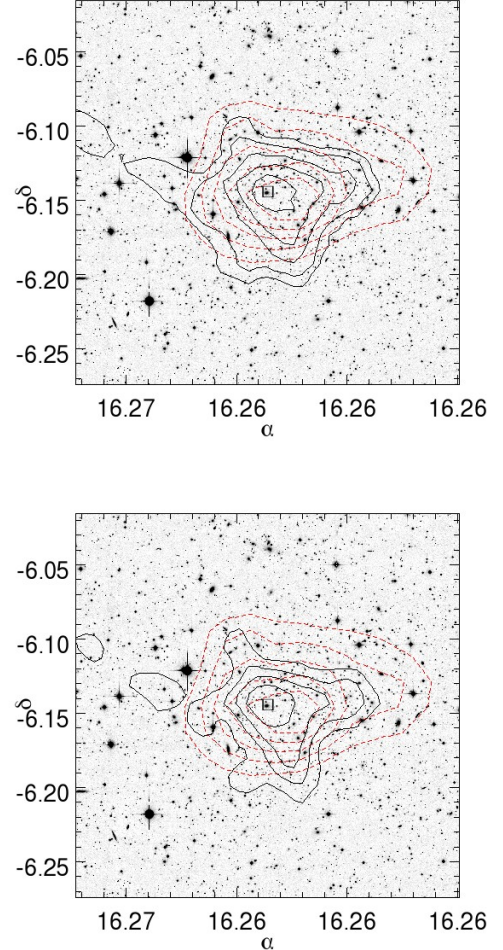


**Fig. 4.**  $S$ -maps obtained by aperture densitometry and convolution with *up*: a Gaussian filter function (size: 5 arcmin); *down*: the filter function proposed by Schirmer (2004). The contour levels are plotted at  $S = (3, 4, 5, 6, 7)$ , where  $S$  is defined in Sec. 3.1.1. The small box indicates the position of the elliptical galaxy with arcs. The dashed contours show for comparison the density distribution of cluster galaxies (see also Maurogordato et al. (2008)).

to fit it as well as a function of the coordinates  $(x, y)$ , using a polynomial of order 2. For each galaxy of size  $r_h$ , we then draw the coefficients computed in the closest bin and finally derive the value of  $\frac{P^{\text{sh}*}}{P^{\text{sm}*}}$ .

The implementation of the KSB procedure is done using a modified version of the Nick Kaiser's IMCAT tools, kindly provided to us by T. Erben (see Hettterscheidt et al. (2007)), which allows to measure the quantities relevant for the lensing analysis starting from catalogs obtained using SExtractor. The package also allows to separate stars and galaxy in the  $r_h$ -mag space and compute the PSF correction coefficients  $P^\gamma$ ,  $p$ . In addition, we

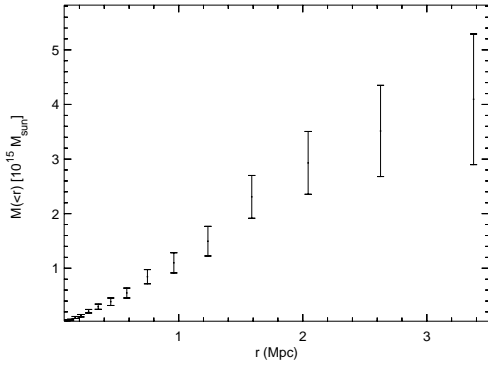


**Fig. 5.** Mass profile obtained by aperture densitometry.

introduced the possibility to fit  $P^\gamma$  vs. the coordinates and use for each galaxy the values of both  $P^\gamma$  and  $p$  computed using the closest value of  $r_h$ .

Stars were selected in the range  $17.5\text{mag} < r < 21\text{mag}$ ,  $0.37'' < r_h < 0.45''$ , giving 2400 stars usable to derive the quantities needed for the PSF correction. As discussed above, these quantities were fitted with a polynomial both for PSF anisotropy and seeing correction: we verified that the behaviour of the PSF across the CCDs allows to use a unique polynomial for the whole image (Fig.3). Galaxies used for shear measurement were selected using the following criteria:  $P_\gamma > 0.25$ ,  $v_{\text{max}} > 5$ ,  $r_h > 0.45''$ ,  $23\text{mag} < r < 25\text{mag}$  and ellipticities smaller than one. We finally obtain  $\sim 17000$  galaxies, the average density of galaxies in the catalog is  $\sim 8$  galaxies/arcmin $^2$ .

The uncertainty on ellipticities is computed as in Hoekstra et al. (2000):

$$w = \frac{1}{\sigma_\gamma^2} = \frac{P^{\gamma^2}}{P^{\gamma^2} \sigma_{e_0}^2 + \langle \Delta e^2 \rangle}, \quad (4)$$

where  $\langle \Delta e^2 \rangle^{1/2}$  is the uncertainty on the measured ellipticity,  $\sigma_{e_0} \sim 0.3$  is the typical intrinsic rms of galaxy ellipticities.

### 3.1. Mass derivation

Weak lensing measures the *reduced shear*  $g = \frac{\gamma}{(1-\kappa)}$ . The convergence  $\kappa$  is defined by  $\kappa = \Sigma/\Sigma_{\text{crit}}$ , where  $\Sigma$  is the surface mass density and  $\Sigma_{\text{crit}}$  is the critical surface density:

$$\Sigma_{\text{crit}} = \frac{c^2}{4\pi G} \frac{D_s}{D_l D_{ls}} = \frac{c^2}{4\pi G} \frac{1}{D_l \beta}, \quad (5)$$

$D_{ls}$ ,  $D_s$  and  $D_l$  being the angular distances between lens and source, observer and source, observer and lens respectively. In the weak lensing approximation,  $\kappa \ll 1$ , so that  $g \sim \gamma$ . However, the measured value of  $\kappa$  includes an unknown additive constant (the so-called *mass-sheet degeneracy*): this degeneracy can be solved either assuming that  $\kappa$  vanishes at the borders of the image, or assuming a mass profile by which the expected shear is known. Both approaches are used here.

For Abell 2163,  $\Sigma_{\text{crit}} = 9.69 \times 10^{13} \beta^{-1} M_\odot \text{ arcmin}^{-2}$ . In our case, we are not able to assign a redshift to each source galaxy; for clusters at low redshifts,  $z \lesssim 0.25$ , it is however possible to assume *single-sheet approximation* that the background galaxies lie at the same redshift (King & Schneider 2001). In order

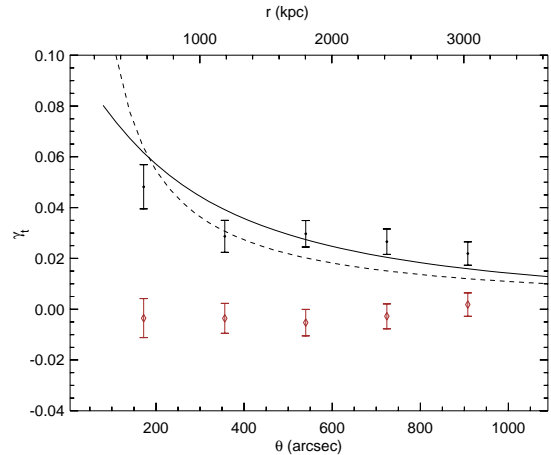


**Fig. 6.** The tangential component of the shear (dark points) is here displayed as a function of the distance from the assumed center of the cluster. The lines show the result of the best-fit on the unbinned data using: a NFW profile with  $c_{\text{vir}}$  given by Eq. 17 (solid line), and a SIS profile (dashed line). Also shown is the radial component of the shear (diamonds), which is expected to be null in the absence of systematic errors.

to estimate this value, we used the publicly available photometric redshifts obtained by Ilbert et al. (2006) for the VVDS F02 field with Megacam photometric data. We applied the same cuts adopted here in the  $r$ -band magnitude and assumed a Gamma probability distribution (Gavazzi et al. 2004):

$$n(z) = z^{a-1} \frac{\exp(-z/z_s)}{\Gamma(a)z_s^a}, \quad (6)$$

We obtain  $a = 2.04$  and  $z_s = 0.57$  as best-fit parameters, and  $\text{Med}(z) = 0.98$ . We therefore adopt a median redshift  $z \sim 1$ , giving  $\langle \beta \rangle = 0.58$ .

#### 3.1.1. Mass aperture maps

Fig. 4 displays the *S-map* introduced by Schirmer et al. (2004), that is:

$$M_{\text{ap}} = \frac{\sum_i e_{t,i} w_i Q(|\theta_i - \theta_0|)}{\sum_i w_i} \quad (7)$$

$$\sigma_{M_{\text{ap}}}^2 = \frac{\sum_i e_{t,i}^2 w_i^2 Q^2(|\theta_i - \theta_0|)}{2(\sum_i w_i)^2}, \quad (8)$$

where  $e_{t,i}$  are the tangential components of the ellipticities of lensed galaxies computed taking as the centre the position in the grid,  $w_i$  are the weights defined in Eq.4,  $Q$  is the filter function discussed below. The ratio  $S = M_{\text{ap}}/\sigma_{M_{\text{ap}}}$ , defined as the *S-statistics* by Schirmer et al. (2004), provides a direct estimate of the signal to noise ratio of the halo detection.

For the window function, we tried two possibilities: a Gaussian function and a function close to a NFW profile.

The Gaussian window function is:

$$Q(|\theta - \theta_0|) = \frac{1}{\pi \theta_c^2} \exp\left(-\frac{(\theta - \theta_0)^2}{\theta_c^2}\right) \quad (9)$$

Schirmer (2004) proposed a filter function whose behaviour is close to that expected from a NFW profile:

	$r_{\text{vir}}$ (kpc)	$M_{\text{vir}}$ ( $10^{14} M_{\odot}$ )	$r_{200}$ (kpc)	$M_{200}$ ( $10^{14} M_{\odot}$ )	$r_{500}$ (kpc)	$M_{500}$ ( $10^{14} M_{\odot}$ )	$r_{2500}$ (kpc)	$M_{2500}$ ( $10^{14} M_{\odot}$ )
NFW	$3012 \pm 170$	$22 \pm 4$	$2362 \pm 130$	$18 \pm 3$	$1514 \pm 90$	$12 \pm 2$	$623 \pm 40$	$4.2 \pm 0.7$
SIS		$18 \pm 5$		$14 \pm 4$		$9 \pm 2$		$4 \pm 1$
A.D.		$38 \pm 10$		$33 \pm 7$		$20 \pm 3$		$5.8 \pm 0.8$

**Table 2.** Best-fit values obtained from the fit of the shear from the NFW model ( $c = 4.09$ ). For comparison, the lower rows give the masses computed at the same radii from the best-fit SIS model ( $\sigma_v = 1139^{+53}_{-56}$  km/s,  $\theta_e = 22''$ ) and from aperture mass densitometry (A.D.).

$$Q(x) = \left(1 + e^{a-bx} + e^{-c+dx}\right)^{-1} \frac{\tanh(x - x_c)}{\pi\theta_0^2(x - x_c)}, \quad (10)$$

where  $x = \theta/\theta_0$  and we adopted the following parameters:  $a = 6$ ,  $b = 150$ ,  $c = 47$ ,  $d = 50$ ,  $x_c = 0.15$  (Hettterscheidt et al. 2005).

In both cases we consistently obtained that (i) the peak of the lensing signal is consistent with the position of the bright elliptical galaxy with the arcs (BCG hereafter), confirming that this is the centre of the mass distribution as already indicated by the X-ray maps and (ii) the weak lensing signal is elongated in the E-W direction: a comparison with Fig.5 and Fig.9 in Maurogordato et al. (2008) shows that the mass distribution follows the density distribution of early-type cluster galaxies (the A1 and A2 substructures).

### 3.1.2. Aperture densitometry

We first estimate the mass profile in the cluster by computing the  $\zeta$  statistics (Fahlman et al. (1994), Clowe et al. (1998)):

$$\zeta(\theta_1) = \bar{\kappa}(\theta \leq \theta_1) - \bar{\kappa}(\theta_2 < \theta \leq \theta_{\text{max}}) = 2 \int_{\theta_1}^{\theta_2} \langle \gamma_T \rangle d \ln \theta \quad (11)$$

$$+ \frac{2}{1 - (\theta_2/\theta_{\text{max}})^2} \int_{\theta_2}^{\theta_{\text{max}}} \langle \gamma_T \rangle d \ln \theta$$

The quantity  $M_{\text{ap}}(\theta_1) = \pi\theta_1^2\zeta(\theta_1)\Sigma_{\text{crit}}$  provides a lower limit on the mass inside the radius  $\theta_1$ , unless  $\bar{\kappa}(\theta_2, \theta_{\text{max}}) = 0$ . This formulation of the  $\zeta$  statistics is particularly convenient as it allows to choose the size of the control annulus ( $\theta_2, \theta_{\text{max}}$ ) so that this condition is reasonably satisfied: in addition, the mass computed in a given aperture does not depend on the mass profile of the cluster (Clowe et al. 1998). Clowe et al. (2004) discussed how the mass estimated by aperture densitometry is affected by asphericity and projected substructures in clusters, as in the case of Abell 2163: they found that the error is less than 5%.

The cluster X-ray emission is detected up to  $2.2h^{-1}$  Mpc (Squires et al. 1997), which corresponds to  $\sim 900''$ . We took advantage of the large available area and chose  $\theta_2 = 1300''$ ,  $\theta_{\text{max}} \sim 1500''$ , giving  $\sim 3000$  sources in the control annulus. The mass profile is displayed in Fig.5, whereas mass values computed at different radii are shown in Table 2.

### 3.1.3. Parametric models

In this section we consider a Singular Isothermal Sphere (SIS) and a Navarro Frenk White (NFW) mass profile, for which the expected shear can be expressed analytically. The fitting of the models is done by minimizing the log-likelihood function (Schneider et al. 2000):

$$l_{\gamma} = \sum_{i=1}^{N_{\gamma}} \left[ \frac{|\epsilon_i - g(\theta_i)|^2}{\sigma^2[g(\theta_i)]} + 2 \ln \sigma[g(\theta_i)] \right], \quad (12)$$

with  $\sigma[g(\theta_i)] = (1 - g(\theta_i)^2)\sigma_e$ .

In the case of a SIS profile, the shear is related to the velocity dispersion  $\sigma$  by:

$$\gamma_t(\theta) = \frac{2\pi\sigma^2 D_{ls}}{\theta c^2 D_s} = \frac{\theta_E}{\theta} \quad (13)$$

In the Navarro Frenk White (NFW) model, the mass profile is (Wright & Brainerd 2000):

$$\rho(r) = \frac{\delta_c \rho_c}{(r/r_s)(1 + r/r_s)^2}, \quad (14)$$

where  $\rho_c = 3H^2(z)/(8\pi G)$  is the critical density of the universe at the redshift of the cluster,  $r_s$  is a characteristic radius related to the virial radius by the concentration parameter  $c_{\text{vir}} = r_{\text{vir}}/r_s$  and  $\delta_c$  is a characteristic overdensity of the halo:

$$\delta_c = \frac{\Delta_{\text{vir}}}{3} \frac{c^3}{\ln(1+c) - c/(1+c)}, \quad (15)$$

$$\Delta_{\text{vir}} \sim (18\pi^2 + 82(\Omega_M(z) - 1) - 39(\Omega_M(z) - 1)^2)/\Omega_M(z).$$

The mass of the halo is:

$$M_{\text{vir}} = \frac{4}{3} \pi \Delta_{\text{vir}} \rho_c r_{\text{vir}}^3 \quad (16)$$

Bullock et al. (2001) used simulations of clusters to show that the virial mass and the concentration are linked by the relation:

$$c_{\text{vir}} = \frac{K}{1+z} \left( \frac{M_{\text{vir}}}{M_{\star}} \right)^{\alpha}, \quad (17)$$

with  $M_{\star} = 1.5 \times 10^{13}/h M_{\odot}$ ,  $K = 9$ ,  $\alpha = -0.13$ .

Comerford & Natarajan (2007) computed the values of  $K$  and  $\alpha$  fitting Eq. 17 to the values of virial mass and concentration measured in a sample of 100 clusters; they adopted  $M_{\star} = 1.3 \times 10^{13} h^{-1} M_{\odot}$  and found  $K = 14.5 \pm 6.4$ ,  $\alpha = -0.15 \pm 0.13$ , which gives values of the concentration  $\sim 1.6$  higher than using the relation proposed by Bullock et al. (2001). Given the high uncertainty in the value of  $K$ , we preferred to adopt the values from Bullock et al. (2001). We used the expression of the shear  $\gamma_t(r)$  derived by Bartelmann (1996); the minimization in Eq. 12 was done using the MINUIT package. Fig. 6 shows the results of the fit and, for comparison, the binned values of the tangential and radial components of the shear: these are consistent with zero, as expected in the absence of systematic effects. Table 2 shows the masses obtained with model fitting (SIS and NFW), as well as those obtained by aperture mass densitometry, at different distances from the BCG assumed to be the center of the cluster. In

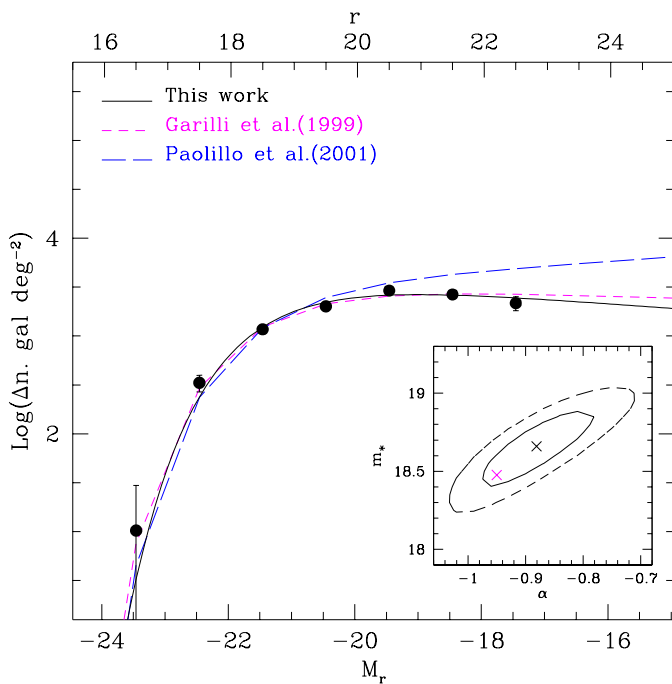


**Fig. 7.** The  $r$  band LF of Abell 2163 compared with other determinations from literature.

	Best-fit	68%	95%
$\alpha$	-0.88	0.09	0.15
$m_*$	18.66	0.23	0.40
$\Phi_*/10^3$	3.8		
$a$	3.19		
$b$	0.36		
$c$	-0.022		

**Table 3.** Best-fit parameters and errors.  $a$ ,  $b$  and  $c$  describe the shape of galaxy counts, whereas  $\alpha$ ,  $m_*$  and  $\Phi_*$  describe the shape of the cluster LF.  $a$ ,  $b$ ,  $c$  and  $\Phi_*$  are in units of  $deg^{-2}$ . The last two columns show the half width of the 68% and 95% confidence range, with two degrees of freedom.

In addition to  $M_{vir}$ , the masses obtained for  $\rho/\rho_c = 200, 500, 2500$  and the corresponding radii  $r_{200}$ ,  $r_{500}$  and  $r_{2500}$ , are also displayed. The value of the virial mass,  $M_{vir} = (22 \pm 4) \times 10^{14} M_\odot$ , confirms Abell 2163 as a massive cluster compared to other clusters (Comerford & Natarajan 2007).

#### 4. Luminosity function

In order to compute the total  $r$ -band luminosity of the cluster and hence the  $M/L$  ratio, we first derived its luminosity function (LF hereafter). The  $r$ -band magnitudes were corrected for Galactic reddening as explained in Sect. 2; no  $k$ -correction was applied since it is negligible at the redshift of Abell 2163, according to Yasuda et al. (2001).

We defined the cluster region as the circular area encompassed within  $r_{200}$  ( $\sim 0.2$  deg, see Table 2) and centered on the BCG. For the control field, we considered the galaxies falling in the outer side ( $\sim 0.36$  deg<sup>2</sup>) of a squared region centered on the BCG with an area of about 0.25 deg<sup>2</sup>.

With this choice, we are confident to minimize the contamination of cluster galaxies and to take into account background

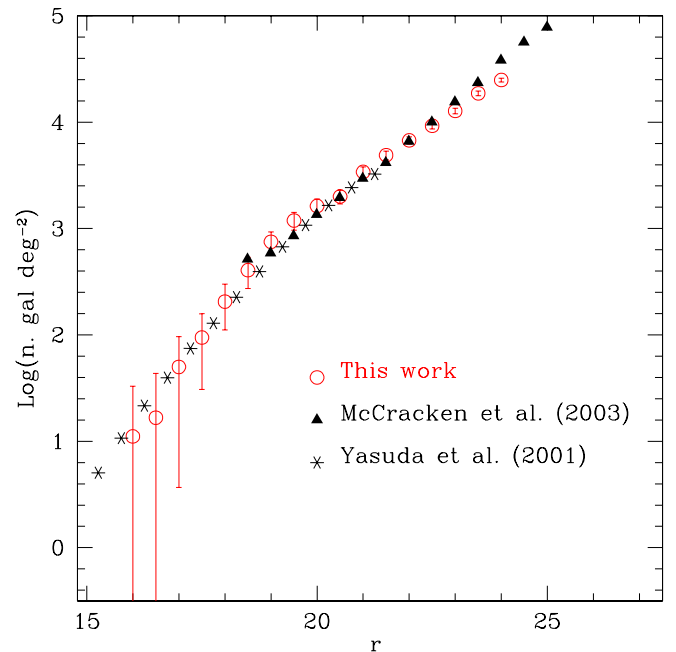


**Fig. 8.** Galaxy counts derived from the control field (empty red circles), compared to literature. The triangles represent the deep counts from the CFH12K-VIRMOS field (McCracken et al. 2003) corrected to the  $r_{AB}$  according to Fukugita et al. (1995); the stars mark the counts from the SDSS commissioning data (Yasuda et al. 2001). The error bars of this work take into account only the Poissonian errors ( $\sqrt{n}/area$ ), whereas for the literature counts the errors are not displayed because smaller than the points dimensions.

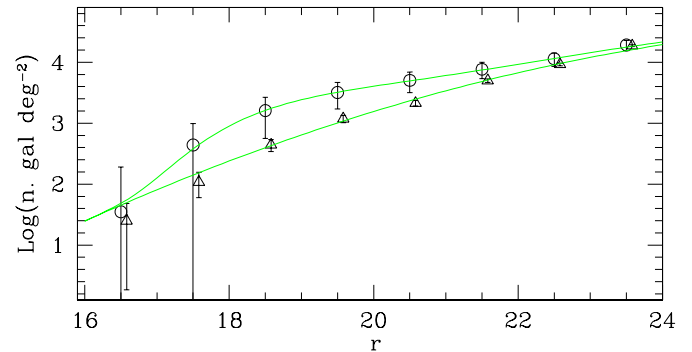


**Fig. 9.** Galaxy counts in the Abell 2163 line of sight (circles) and in the control field (triangles: for display purposes, an offset in  $r$  was applied to these points). The lines show the result of the joint fit. The errors bars were computed as described in the text.

non uniformities on the angular scale of the cluster. Fig. 8 shows that the  $r$ -band galaxy counts in the control field are consistent with those found in literature.

The LF was computed by fitting the galaxy counts in the cluster and control field areas: we adopted the rigorous approach introduced by Andreon et al. (2005), which allows to include at the same time in the likelihood function to be minimized the contributions from both background and cluster galaxies. As the model for the counts of the cluster field, we used the sum of a power law (the background contribution in the cluster area) and a Schechter (1976) function, normalized to the cluster area  $\Omega_{cl}$ :

$$p_{cl,i} = \Omega_{cl} \Phi_{\star} 10^{0.4(\alpha+1)(m_{\star}-m)} \exp(-10^{0.4(m_{\star}-m)}) + \Omega_{cl} 10^{a+b(m-20)+c(m-20)^2}. \quad (18)$$

For the control field this reduces to the power law only, normalized to the background area  $\Omega_{bkg}$ :

$$p_{bkg,i} = \Omega_{bkg} * 10^{a+b(m-20)+c(m-20)^2}. \quad (19)$$

$\Phi_{\star,\alpha}$  and  $m_{\star}$  are the Schechter parameter as usually defined.  $a, b, c$  describe the shape of the galaxy counts in the reference field direction and the value of 20 was chosen for numerical convenience.

Best-fitting parameters (see Table 3) were determined simultaneously by using a conventional routine of minimization on the unbinned distributions, whereas the data were binned for display purpose only. The best-fit is shown in Fig.9, showing the binned galaxy counts in the control field (empty triangles) and cluster (empty circles) areas; the joint fit to the unbinned data sets is also overplotted. Error bars are computed by  $\sqrt{n}/\Omega$ . In order to check the effect of the uncertainty in the position-dependent extinction correction (see Sec. 2), we computed the same parameters in a set of catalogs where for each the galaxy the extinction correction was randomly modified within  $\pm 15\%$ , the expected uncertainty in  $E(B - V)$  (Schlegel et al. 1998): the rms in the so-obtained parameters is negligible compared to the uncertainties on the fit. Fig.7 displays the derived LF compared with selected determinations from literature, converted to our cosmology.

We compare our LF with Garilli et al. (1999) and with Paolillo et al. (2001), which use data calibrated to the Thuan & Gunn photometric system; for all these works we found null or not relevant conversions between the magnitude system they used and our (following Fukugita et al. (1995)).

Our determination of LF shows a good level of agreement with Garilli et al. (1999) (inside the 68% confidence level, see Fig. 7) and is compatible with the  $M_{\star}$  of Paolillo et al. (2001).

The  $r$ -band total luminosity was calculated by  $L_{tot} = L_{\star} \phi_{\star} \Gamma(2 + \alpha)$ . The transformation from absolute magnitudes  $M_{\star}$  to absolute luminosity  $L_{\star}$  in units of solar luminosities was performed using the solar absolute magnitude obtained from the color transformation equation from the Johnson-Morgan-Cousins system to the SDSS system of Fukugita et al. (1995). The errors were estimated by the propagation of the 68%-confidence-errors of each parameter. In this way we found  $L_{tot} = (80 \pm 2) \times 10^{11} L_{\odot}$ , that gives  $M_{200}/L_{tot} \sim 230$  ( $M_{200} = 1.8 \times 10^{15} M_{\odot}$ , Table 2). Popesso et al. (2007) found a relation between  $M_{200}$  and the  $r$ -band luminosity in 217 clusters selected from the Sloan Digital Sky Survey (see their Eq. 6): according to this relation, the luminosity expected for  $M_{200} = 1.8 \times 10^{15} M_{\odot}$  is  $L = (73 \pm 10) \times 10^{11} L_{\odot}$ , in excellent agreement with the observed value.

## 5. Conclusions

We showed that using wide-field images it is possible to achieve for Abell 2163 a much better consistency of the mass and velocity dispersion with the values obtained e.g. by X-ray data, compared to previous results.

The dispersion velocity here obtained,  $\sigma = 1139_{-55}^{+52} \text{ km s}^{-1}$ , confirms the result by Cypriano et al. (2004): this value is in good agreement with the one given by X-ray and spectroscopic data, whereas it was underestimated in the previous analysis by Squires et al. (1997).

On the other hand, the comparison with the masses obtained from X-ray measurements (Markevitch et al. 1996) shows that at  $r \sim 2 \text{ Mpc}$ ,  $M_X \sim (1.5 \pm 0.2) \times 10^{15} M_{\odot}$  ( $h = 0.7$ ); at the same distance, we obtain from the NFW fit (sec.3.1.3)  $M_{wl} \sim (1.6 \pm 0.3) \times 10^{15} M_{\odot}$ . We therefore agree with Squires et al. (1997) on the consistency of the mass obtained by weak lensing and X-rays: no correction factor is required in our case due to the larger field of view. We also find a substantial agreement between our estimate of the virial mass,  $M_{vir} = (2.2 \pm 0.4) \times 10^{15} M_{\odot}$  using the NFW fit, and the value  $M_{vir} = (3.8 \pm 0.4) \times 10^{15} M_{\odot}$  obtained by Maurogordato et al. (2008) from optical and spectroscopic data; in addition, as noted by the authors, this value could be overestimated by 25%. Our weak lensing analysis also confirms that the mass distribution is extended along the E-W direction, in agreement with what observed in optical, radio and X-ray data (see e.g. Maurogordato et al. (2008)).

Finally, the  $r$ -band total cluster luminosity within  $r_{200}$ , derived from the luminosity function, gives  $L_{tot}/M_{200} = 240$ . The observed luminosity is in very good agreement with the one expected for the mass measured by weak lensing, according to the  $L - M$  relation proposed by Popesso et al. (2007).

*Acknowledgements.* We warmly thank Thomas Erben for having provided us the software for the KSB analysis. E. Puddu thanks S. Andreon for useful suggestions and comments about the LF determination. We are grateful to the referee for his comments, which improved the paper. This research is based on observations made with the Canada-France Hawaii Telescope obtained using the facilities of the Canadian Astronomy Data Centre operated by the National Research Council of Canada with the support of the Canadian Space Agency. This research was partly based on the grant PRIN INAF 2005.

## References

- Abell, G., Corwin, H., & Olowin, R. 1989, ApJS, 70, 1  
 Andreon, S., Punzi, G., & Grado, A. 2005, MNRAS, 360, 727  
 Arnaud, M., Elbaz, D., Böhringer, H., Soucail, G., & Mathez, G. 1994, in New Horizon of X-Ray Astronomy, ed. F. Makino & T. Ohashi (Tokyo: Universal Academy Press), 537  
 Arnaud, M., Hughes, J. P., Forman, W., et al. 1992, ApJ, 390, 345  
 Bartelmann, M. 1996, A&A, 313, 697  
 Bullock, J. S., Kolatt, T. S., Sigad, Y., et al. 2001, MNRAS, 321, 559  
 Clowe, D., DeLucia, G., & King, L. 2004, MNRAS, 350, 1038  
 Clowe, D., Luppino, G. A., Kaiser, N., Henry, J. P., & Gioia, I. M. 1998, ApJ, 497, L61  
 Comerford, J. M. & Natarajan, P. 2007, MNRAS, 379, 190  
 Cypriano, E. S., Sodr , L. J., Kneib, J.-P., & Campusano, L. E. 2004, ApJ, 613, 95  
 Elbaz, D., Arnaud, M., & Boehringer, H. 1995, A&A, 293, 337  
 Fahlman, G., Kaiser, N., Squires, G., & Woods, D. 1994, ApJ, 437, 56  
 Feretti, L., Fusco-Femiano, R., Giovannini, G., & Govoni, F. 2001, A&A, 373, 106  
 Feretti, L., Orr , E., Brunetti, G., et al. 2004, A&A, 423, 111  
 Fukugita, M., Shimasaku, K., & Ichikawa, T. 1995, PASP, 107, 945  
 Garilli, B., Maccagni, D., & Andreon, S. 1999, A&A, 342, 408  
 Gavazzi, R., Mellier, Y., Fort, B., Cuillandre, J.-C., & Dantel-Fort, M. 2004, A&A, 422, 407  
 Herbig, T. & Birkinshaw, M. 1994, AAS  
 Hettterscheidt, M., Erben, T., Schneider, P., et al. 2005, A&A, 442, 43  
 Hettterscheidt, M., Simon, P., Schirmer, M., et al. 2007, A&A, 468, 859  
 Hoekstra, H., Franx, M., & Kuijken, K. 2000, ApJ, 532, 88  
 Hoekstra, H., Franx, M., Kuijken, K., & Squires, G. 1998, ApJ, 504, 636  
 Ilbert, O., Arnouts, S., McCracken, H. J., et al. 2006, A&A, 457, 841  
 Kaiser, N., Squires, G., & Broadhurst, T. 1995, ApJ, 449, 460  
 King, L. J. & Schneider, P. 2001, A&A, 369, 1  
 Luppino, G. & Kaiser, N. 1997, ApJ, 475, 20  
 Markevitch, M., Mushotzky, R., Inoue, H., et al. 1996, ApJ, 456, 437  
 Martini, P., Mulchaey, J. S., & Kelson, D. D. 2007, ApJ, 664, 761  
 Maurogordato, S., Cappi, A., Ferrari, C., et al. 2008, ArXiv:0712.2715  
 McCracken, H., Radovich, M., Bertin, E., et al. 2003, A&A, 410, 17  
 Miralda-Escude, J. & Babul, A. 1995, ApJ, 449, 18  
 Paolillo, M., Andreon, S., Longo, G., et al. 2001, A&A, 367, 59  
 Popesso, P., Biviano, A., Böhringer, H., & Romaniello, M. 2007, A&A, 464, 451

- Radovich, M., Arnaboldi, M., Ripepi, V., et al. 2004, *A&A*, 417, 51
- Schirmer, M. 2004, PhD thesis, Univ. Bonn
- Schirmer, M., Erben, T., Schneider, P., Wolf, C., & Meisenheimer, K. 2004, *A&A*, 420, 75
- Schlegel, D., Finkbeiner, D., & Davis, M. 1998, *ApJ*, 500, 525
- Schneider, P., King, L., & Erben, T. 2000, *A&A*, 353, 41
- Squires, G., Neumann, D. M., Kaiser, N., et al. 1997, *ApJ*, 482, 648
- Wright, C. O. & Brainerd, T. G. 2000, *ApJ*, 534, 34
- Yasuda, N., Fukugita, M., Narayanan, V., et al. 2001, *AJ*, 122, 1104